

Boron-doped boron oxynitride photocatalyst for visible light-driven H₂ evolution and CO₂ photoreduction

Ravi B. Shankar^a, Daphné Lubert-Perquel^{b,†}, Elan D. R. Mistry^c, Irena Nevjestic^b, Sandrine Heutz^b and Camille Petit^{a*}

^aBarrer Centre, Department of Chemical Engineering, Imperial College London, South Kensington Campus, Exhibition Road, London SW7 2AZ, United Kingdom

^bLondon Centre for Nanotechnology and Department of Materials, Imperial College London, South Kensington Campus, Prince's Consort Road, London SW7 2BP, United Kingdom

^cDepartment of Chemistry, Imperial College London, South Kensington Campus, Exhibition Road, London SW7 2AZ, United Kingdom

[†]Current address: National High Magnetic Field Laboratory, Tallahassee, FL 32306 (U.S.A.)

*Corresponding author:

E-mail: camille.petit@imperial.ac.uk; Phone: +44 (0)20 7594 3182 (C. Petit)

Abstract

Developing robust, multifunctional photocatalysts that can facilitate both hydrogen evolution *via* photoreforming of water and gas phase CO₂ photoreduction is highly desirable with the long-term vision of integrated photocatalytic setups. Here, we present a step-change in the family of boron oxynitride materials by introducing the first example of a B-doped boron oxynitride (B-BNO). This material resolves an on-going bottleneck associated with BN-based materials, i.e. the lack of photoactivity under visible light. Detailed EPR studies revealed distinct hyperfine interactions between the free oxygen radicals and 3 neighbouring boron nuclei. This confirmed isolated OB₃ sites, which contribute to band gap narrowing, as the radical species and origin of paramagnetism in BNO materials. We show that B-BNO can facilitate both liquid phase H₂ evolution and gas phase CO₂ photoreduction, using UV-Vis and deep visible irradiation ($\lambda > 550$ nm), without any co-catalysts. The evolution rates, quantum efficiencies, and selectivities observed for both reactions with B-BNO exceed those of its porous BNO counterpart, P25 TiO₂ and bulk g-C₃N₄.

Keywords: boron nitride, photocatalysis, boron doping, solar fuels, H₂ evolution, CO₂ photoreduction

Introduction

With the ongoing efforts to stem the flow of anthropogenic CO₂ emissions, the share of renewables is projected to increase in the years and decades to come in the quest to transition from a fossil fuel dominant energy infrastructure to a sustainable energy portfolio.¹ The solar-driven production of fuels and valuable chemicals *via* photocatalysis represents one such energy generation route, allowing one to directly harness the abundance of incident sunlight. Common solar fuels obtained through this technology include H₂ derived from water splitting or photoreforming of water, and carbon-based molecules (e.g. CO, CH₄, CH₃OH, etc...) derived from CO₂ photoreduction.² Aside from solar fuel production, there have been efforts to utilize photocatalysis to synthesize other feedstock commodity chemicals, such as ammonia (NH₃) *via* photocatalytic nitrogen fixation^{3, 4} and hydrogen peroxide (H₂O₂) *via* the solar-driven anthraquinone process.⁵

In contrast to studies pertaining to H₂ evolution *via* photocatalytic water splitting, which have been rife since the pioneering works of Fujishima and Honda⁶ and Inoue *et al.*,⁷ literature on catalysts for CO₂ photoreduction is comparatively less extensive. Indeed, the multiple electron transfer mechanism required for CO₂ photoreduction certainly presents increased thermodynamic barriers and kinetic limitations to overcome in comparison to water splitting, which only requires a two-electron transfer process. Designing robust photocatalysts from earth abundant elements, which can efficiently harness sunlight to drive this heterogeneous photocatalytic reaction, remains an on-going challenge in the field of solar fuels synthesis. To this end, researchers have investigated a plethora of materials, both porous and non-porous, as potentially viable photocatalysts. Examples of such materials include: derivatives of TiO₂,⁸⁻¹² metal oxides,^{11, 13-15} oxynitrides,¹⁶⁻¹⁹ carbon nitrides,²⁰⁻²⁵ metal organic frameworks,^{8, 10, 26} covalent organic frameworks,²⁷⁻²⁹ linear conjugated polymers,³⁰⁻³³ and composites thereof.^{8, 10, 25, 34}

In a recent study, we focused on porous boron oxynitride (BNO),³⁵ a material that is gaining attention in the photocatalysis community.^{21, 25, 35-42} Porous BNO exhibits key properties of an ideal photocatalyst, with the compelling features being its tuneable chemistry/photochemistry,

which facilitate a tailored band structure *a priori*.⁴³ However, prior to this work,³⁵ porous BNO had never been studied for CO₂ photoreduction. In our proof-of-concept study, we reported a porous BNO material that could function simultaneously as an adsorbent and semiconductor to facilitate combined gas phase CO₂ capture and photoreduction, using both UV and visible light, under ambient conditions without any co-catalyst. We showed that the rate performance of CO₂ photoreduction to CO with porous BNO was higher than that of the benchmark in the field, *i.e.* P25 TiO₂.

The results from this work have enabled to introduce porous BNO as a new platform photocatalyst material. However, the material presented a key bottleneck that limits its application and performance, namely the limited photoactivity exhibited by porous BNO in the visible region of the light spectrum. Whilst porous BNO indeed facilitated CO₂ photoreduction to CO under pure visible light, the rate performance was much lower compared to UV-Vis irradiation. With 55% of the solar spectrum concentrated as visible light, it is essential to expand the BN photocatalyst functionality to deeper within the visible-light region, and thereby increase its rate performance. We therefore pose the key research question that frames this study: *can we synthesize a BNO material that harvests light across the visible region of the spectrum?*

With this in mind, we expand the BN photocatalyst material platform by studying boron-doped boron oxynitride (B-BNO) for both H₂ generation and CO₂ photoreduction. This material exhibits semiconducting properties and photophysics not previously observed in BN materials. Hyperfine interactions in B-BNO between the unpaired electron from oxygen atoms and the nuclear spin of neighbouring boron atoms were observed in room temperature EPR spectra. The results showed that the oxygen radical is interacting with three boron nuclei. This confirmed our previous hypothesis³⁵ that the paramagnetic signature originates from isolated OB₃ sites, which play an important role in extending the band gap to the deep visible range in BNO materials. The free radical in these isolated OB₃ sites exhibits an out-of-plane symmetry, akin to a 2p_z antibonding orbital. The presence of hyperfine interactions further provided

valuable, direct insight into the structure and chemistry of this new B-BNO material. As a progression from our proof-of-concept study,³⁵ we show that B-BNO can overcome the bottleneck associated to the benchmark BN photocatalyst, porous BNO, namely the lack of light harvesting in the visible region. In doing so, B-BNO can facilitate H₂ evolution *via* the photoreforming of water in a simple solid/liquid phase set-up under ambient conditions, without the use of a co-catalyst. In addition, B-BNO can serve as a multifunctional photocatalyst and photoreduce CO₂ to CO in the gas phase under both UV-Vis and deep visible ($\lambda > 550$ nm) irradiation, with evolution rates higher than porous BNO, P25 TiO₂, and bulk graphitic carbon nitride (g-C₃N₄). This is first time that a BN-based material is able to function as a semiconductor to facilitate both liquid phase H₂ evolution and CO₂ photoreduction, under both UV-Vis and deep visible irradiation, without the use of additional element dopants (outside of the constituent B, N and O atoms) or co-catalysts. This work could pave the way for the expansion and further development of the BN photocatalyst platform.

Materials and methods

We synthesized boron-doped BNO (B-BNO) through a two-step procedure, based on the previous work of Weng *et al.*⁴³ and Rusanova and Gorchakova,⁴⁵ as outlined below. The first step relies on the bottom-up synthesis of oxygen-doped boron nitride (BNO) using a mixture of boric acid and hexamethylenetetramine under an ammonia atmosphere at 1000 °C, as outlined by Weng *et al.*⁴³ The second step, outlined by Rusanova and Gorchakova,⁴⁵ involves the nitrification of amorphous boron in the presence of the as-synthesized BNO under an inert nitrogen atmosphere at elevated temperatures (>1300 °C) for prolonged time periods.

Synthesis of boron-doped boron oxynitride (B-BNO). The first step involves the bottom-up synthesis of oxygen-doped boron nitride (BNO) based on the procedure of Weng *et al.*⁴³ In a typical synthesis, boric acid (20 mmol, 1.237 g) (H₃BO₃, ACS reagent, 99.0 %, Sigma-Aldrich) and hexamethylenetetramine (HMTA) (40 mmol, 5.607 g) (C₆H₁₂O₆, molecular biology

grade, Sigma-Aldrich) were added to deionized water (100 mL) at 90 °C under rapid stirring to form a boric acid-HMTA complex in solution. The solution was allowed to evaporate overnight until the resulting white powder was collected and subsequently dried for 24 hours at 90 °C in a drying oven. The dried material (approx. 1.4 g) was transferred to an alumina boat crucible, which was placed in a horizontal tubular furnace. The sample was initially degassed at ambient temperature for 30 minutes under pure ammonia flow, with the flowrate set to flow rate of 250 cm³ min⁻¹. Once the degas was complete, the ammonia flow rate was decreased to 150 cm³ min⁻¹, and the sample was heated from ambient temperature to 1000 °C with a ramp rate of 10 °C min⁻¹. This steady-state temperature was maintained for 3 hours, after which the samples were allowed to naturally cool to approximately 600 °C under the same ammonia flow rate. At this point, the ammonia flow was shut off and inert argon gas was flowed through at a rate of 100 cm³ min⁻¹ overnight until the furnace had cooled to room temperature. Upon completion of the synthesis, a yellow powder was obtained, which we refer to as BNO. The yellow colour originates from the O atoms.⁴³

The second step of the synthesis involves the nitrification of amorphous boron in the presence of the as-synthesized BNO sample, according to Rusanova and Gorchakova.⁴⁵ The as-synthesized BNO sample and amorphous boron powder (>95%, Sigma Aldrich) in a ratio of 75 wt.% : 25 wt.% were mechanically mixed in an agate mortar to form a homogeneous powder, and then transferred to an alumina crucible, which was placed in a horizontal tubular furnace. The furnace was purged under nitrogen flow with a flow rate of 100 cm³ min⁻¹ overnight after which the sample was heated from ambient temperature to 1500 °C with a ramp rate of 10 °C min⁻¹ under the same nitrogen flow rate. This steady-state temperature was maintained for 10 hours, after which the sample was allowed to naturally cool to room temperature, whilst maintaining the same flowrate of nitrogen. Upon completion of the synthesis, a light grey powder product was obtained, which we refer to as B-BNO. We chose a synthesis temperature of 1500 °C based on the results of Rusanova and Gorchakova,⁴⁵ who

showed that full nitrification of amorphous boron was achieved for a synthesis temperature of 1500 °C. We selected a reaction time of 10 hours for the same reason.

Synthesis of porous BNO. Porous BNO synthesis was based on the method developed by Marchesini *et al.*⁴⁶ In a typical synthesis, boric acid (10 mmol, 0.6177 g) (H_3BO_3 , ACS reagent, 99.0 %, Sigma-Aldrich), urea (50 mmol, 3.000 g) ($\text{CH}_4\text{N}_2\text{O}$, molecular biology grade, Sigma-Aldrich), and melamine (10 mmol, 1.261 g) ($\text{C}_3\text{H}_6\text{N}_6$, ACS reagent, 99.0 %, Sigma-Aldrich), with a 1:1 molar ratio of boric acid to melamine and 1:5 molar ratio of boric acid to urea, were mechanically mixed together and finely ground for 5 minutes in an agate mortar to form a homogeneous powder. The finely ground powder was subsequently transferred to an alumina boat crucible, which was placed in a horizontal tubular furnace. The sample was initially degassed at ambient temperature for 3 hours under an inert nitrogen atmosphere (flow rate of $250 \text{ cm}^3 \text{ min}^{-1}$). Once the degas was complete, the nitrogen flow rate was decreased to $50 \text{ cm}^3 \text{ min}^{-1}$, and the sample was heated from ambient temperature to 1050 °C with a ramp rate of $10 \text{ }^\circ\text{C min}^{-1}$. This steady-state temperature was maintained for 3.5 hours, after which the samples were allowed to naturally cool to room temperature, whilst maintaining the same nitrogen flow rate. Upon completion of the synthesis, a porous white powder was obtained, which we refer to as porous BNO.

Synthesis of bulk g- C_3N_4 . In a typical synthesis, melamine (12 g) ($\text{C}_3\text{H}_6\text{N}_6$, ACS reagent, 99.0 %, Sigma-Aldrich) were weighed and transferred to an alumina crucible, which was placed in a muffle furnace. The sample was heated from ambient temperature to 560 °C with a ramp rate of $5 \text{ }^\circ\text{C min}^{-1}$. This steady-state temperature was maintained for 4 hours, after which the sample was allowed to naturally cool to room temperature. Upon completion of the synthesis, a yellow solid product was obtained, which was subsequently ground in an agate mortar to form a fine, homogeneous powder, which we refer to as bulk g- C_3N_4 .

P25 TiO_2 and amorphous boron. P25 TiO_2 and amorphous boron were industrially synthesized and obtained as follows: P25 TiO_2 (Sigma Aldrich, >99.5%, 21 nm primary particle size) and amorphous boron ($\geq 95\%$, Sigma-Aldrich).

Characterization

Fourier transform infrared spectroscopy (FT-IR). The samples were first ground to a powder using an agate mortar. Subsequently, the spectra were obtained in the range of 500 – 4000 cm^{-1} using a Perkin-Elmer Spectrum 100 FT-IR spectrometer equipped with an attenuated total reflectance (ATR) accessory.

X-ray photoelectron spectroscopy (XPS) was employed to determine the relative elemental composition of the samples, the chemical states of the elements, the valence band off-set and secondary electron cut-off was conducted using a Thermo Scientific K-Alpha⁺ X-ray Photoelectron Spectrometer equipped with a MXR3 Al K α monochromated X-ray source ($h\nu = 1486.6$ eV). The samples were initially ground and mounted onto an XPS sample holder using a small rectangular piece of conductive carbon tape. The X-ray gun power was set to 72 W (6 mA and 12 kV). Survey scans were acquired using 200 eV pass energy, 0.5 eV step size and 100 ms (50 ms x 2 scans) dwell times. All of the high resolution core level spectra (B 1s, N 1s, and O 1s) were obtained using a 20 eV pass energy and 0.1 eV step size. The valence band spectra were obtained using a 15 eV pass energy and 0.05 eV step size. The results were analysed using the Thermo Avantage data analysis program. Any charging effect in the core level and valence band measurements was mitigated by using a dual-beam flood gun that uses the combination of low energy electrons and argon ions.

UV-Vis diffuse reflectance (UV-Vis DR) spectroscopy. UV-Vis DR spectroscopy was conducted using a Shimadzu UV-2600 true optical double beam UV-Vis spectrophotometer equipped with an integrating sphere. The integrating sphere has an InGaAs detector with a detection range of 220 – 1400 nm. Spectral band width was set to 5 nm and barium sulphate (BaSO_4) was used as a standard for the baseline corrections. Spectra were treated using Kubelka-Munk function in order to eliminate any tailing contribution from the UV-Vis DR spectra. The following equation was applied: $F(R) = (1-R)^2/2R$ where R is the reflectance (%). The band gaps (E_G) were estimated *via* extrapolation of the linear section of the Tauc plot

of $[F(R).hv]^{1/n}$ against photon energy ($h\nu$). We consider BNO and m-BNO as direct band gap ($n = 0.5$) semiconductors based on literature.⁴⁷

Powder X-ray diffraction (XRD) was performed using a PANalytical X'Pert Pro X-ray diffractometer in reflection-transmission mode with a spinning stage (2 revolutions/second). An anode voltage of 40 kV and emission current of 20 mA were chosen as the operating conditions using a monochromatic Cu-K α radiation source ($\lambda = 1.54178$ Å). The X'Celerator silicon strip detector was used in the diffractometer. The interplanar $d_{(002)}$ -spacing was calculated from the powder XRD patterns using Bragg's law.

Nitrogen and CO₂ sorption isotherms were measured using a volumetric sorption analyser (Micrometrics 3 Flex) at -196 °C and 25 °C, respectively. The samples were initially degassed overnight at 140 °C at approximately 0.2 mbar pressure. Prior to the sorption isotherm measurement, the samples were further degassed in-situ for 4 hours at 120 °C. The equivalent specific surface areas of the samples were determined using the Brunauer-Emmett-Teller (BET) method.⁴⁸ The total pore volume was ascertained from the volume of N₂ adsorbed at a relative pressure (P/P_0) of 0.97. The micropore volume was determined using the Dubnin-Radushkevich model.⁴⁹

Photocatalytic H₂ evolution. A liquid/solid Teflon-lined reactor setup was assembled to conduct the photocatalytic H₂ evolution tests. The photocatalyst (10 mg) was dispersed in 25 mL of 0.1 M (aq) triethanolamine (TEOA) solution inside a Teflon vessel with a magnetic stirrer bar. The vessel was inserted into a stainless steel closed reactor. Zero grade (99.998% purity) N₂ was fed at controlled rates using a mass flow controller (Omega Engineering, 0-100 mL min⁻¹). After the reactor was sealed, the system was purged with N₂ for 30 mins. The photoreactor was then vacuumed and replenished with N₂ ten times, after which the reactor was pressurised up to 1.40 bara, sealed and irradiated for 3 hours. A Xe arc lamp (300 W, $\lambda > 325$ nm, LOT Quantum Design), equipped with a water filter was used as the irradiation source with the distance from the lamp to the sample being 12.5 cm. A long pass visible filter ($\lambda < 550$ nm) (Thor Labs) was used to conduct the tests under deep visible light irradiation and

the lamp emission spectra, both with and without the UV filters, are provided in Supplementary Figure 1. The intensity at the catalyst surface was measured to be $1730 \pm 26 \text{ W m}^{-2}$ without the visible filter and $1530 \pm 12 \text{ W m}^{-2}$ with the filter. The lamp intensity was acquired using a UV-Vis spectrophotometer with 280 – 900 nm range (StellarNet) and an average lamp intensity with standard deviation was calculated after three repeat measurements. The evolved gases were detected by a gas chromatograph (GC, Agilent Technologies) with HayeSep and molecular sieve columns in series, and thermal conductivity (TCD) and flame ionisation (FID) detectors. In addition, isotopic tracing experiments were performed with D_2O (Sigma Aldrich, >99.9%). The photocatalytic H_2 evolution tests were repeated three times for each material under the same reaction conditions to obtain an average specific H_2 production rate, from which the standard deviation in the measurements was calculated.

Photocatalytic reduction of CO_2 . A gas/solid photoreactor setup was assembled to conduct the photocatalytic reduction of CO_2 . The as-synthesized, finely ground photocatalysts were deposited on a circular metal disc with a fixed area of 9.6 cm^2 . To do so, 30 mg of photocatalyst (B-BNO, Porous BNO, P25 TiO_2 , and bulk $\text{g-C}_3\text{N}_4$) was added to 1.5 mL of ethanol and stirred rapidly to form a homogeneous suspension, which was drop casted onto the sample holder. The drop casted sample was dried overnight at $120 \text{ }^\circ\text{C}$ in a drying oven prior to testing. Research grade (99.999%) CO_2 and H_2 (99.9995%, Peak Scientific PH200 hydrogen generator) were flowed at controlled rates using mass flow controllers (Omega Engineering, 0–50 mL/min). Firstly, the photoreactor (35 cm^3) was vacuumed and replenished with a gas mixture of CO_2 and H_2 (1.5 vol/vol ratio) ten times. The same gas mixture of CO_2 and H_2 was subsequently passed over the catalyst bed in the photoreactor for 15 residence times before it was sealed at 1.40 bara and irradiated for 3 hours. A xenon arc lamp (300 W, $\lambda > 325 \text{ nm}$, LOT Quantum Design), equipped with a water filter was used as the irradiation source with the distance from the lamp to the sample being 9.5 cm and the intensity at the catalyst surface measured to be $1850 \pm 17 \text{ W m}^{-2}$. The lamp intensity was measured using a UV-Vis spectrophotometer with 280 – 900 nm range (StellarNet) and an average lamp intensity with

standard deviation was calculated after three repeat measurements. The evolved gases were detected by a gas chromatograph (GC, Agilent Technologies) with HayeSep and molecular sieve columns in series, and thermal conductivity (TCD) and flame ionisation (FID) detectors. In addition, isotopic tracing experiments were performed with $^{13}\text{CO}_2$ (BOC, >98% atom $^{13}\text{CO}_2$ compared to $^{12}\text{CO}_2$, >99%). The photocatalytic CO_2 reduction tests were repeated three times for each material under the same reaction conditions to obtain an average specific CO production rate, from which the standard deviation in the measurements was calculated.

Electron paramagnetic resonance (EPR) spectroscopy. EPR experiments were acquired using a Bruker Elexsys E580 CW EPR spectrometer operating at X-band frequencies (9–10 GHz/0.3 T), equipped with a Bruker ER4118-X MD5 resonator. All spectra were recorded at room temperature in air atmosphere in 4mm EPR suprasil tubes. Specifically, the B-BNO data was acquired using a microwave frequency of 9.658 GHz with microwave power 0.2 mW and a 10 Hz modulation with 1G amplitude in the detection sequence. On the other hand, porous BNO measurements required 2 mW power with 100 kHz modulation with 2G amplitude.³⁵ Simulations were carried out using the EasySpin⁵⁰ toolbox running on MATLAB™.

Work function measurements. The work function of B-BNO and porous BNO was determined by measuring the secondary electron cut-off in the low kinetic energy region using a Thermo Scientific K-Alpha⁺ X-ray Photoelectron Spectrometer equipped with a MXR3 Al $K\alpha$ monochromated X-ray source ($h\nu = 1486.6$ eV). A known mass (100 mg) of sample was pelletized to form a thin, homogeneous pellet, which was clipped to the sample holder. The sample holder contained a clean gold standard sample, which was used as a reference material to ensure correct calibration. A bias of -30 V was applied to the samples using a DC supply and the cut-off spectra were obtained using a pass energy of 10 eV. The connection is made at the bottom of the sample holder and the voltage is activated from the sputter window. The data for the secondary electron cut-off has been processed such that the tangent is taken at the segment of the graph where the data exhibits a linear trend after the initial curve upwards

from the x-axis. To do so, we have used linear extrapolation to fit a line of best fit to the linear data range with the corresponding equation and coefficient of determination.

Results and discussion

To gain insight into the morphology and structure of the B-BNO material in comparison to porous BNO, we first collected powder XRD patterns (Figures 1a). The XRD patterns in Figure 1a confirm the enhanced crystallinity of B-BNO in comparison to porous BNO through the sharper peaks at 2θ values of 26° and 44° , corresponding to the (002) and (100) planes, respectively.^{46,51,52} This indicates longer-range 3D/graphitic order in B-BNO in contrast to porous BNO, which exhibits an amorphous/turbostratic nature with significantly broader peaks at the same 2θ values. The d-spacing calculated from the XRD peak (002) for B-BNO and porous BNO is 3.4 Å and 3.5 Å, respectively. The d-spacing in porous BNO is only relevant to the pseudo-crystalline regions of the material.

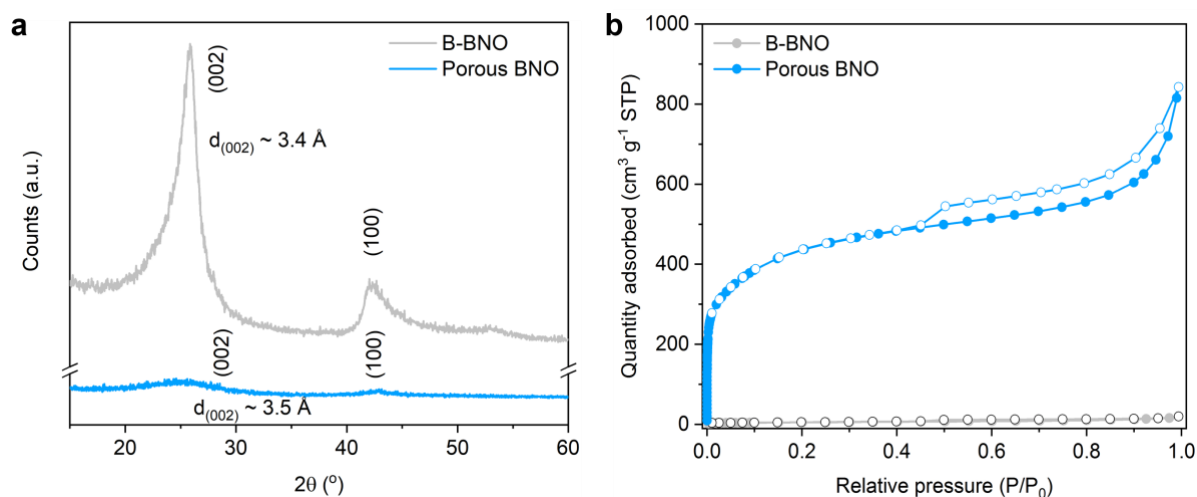


Figure 1 | Structure and morphology of the B-BNO sample compared to porous BNO. (a) Powder XRD patterns of B-BNO and porous BNO and (b) N_2 sorption isotherms for B-BNO and porous BNO measured at -196°C .

To characterize the structural features of the material at the micro/nano-scale, we analyzed the specific surface area and porosity through nitrogen sorption at $-196\text{ }^{\circ}\text{C}$ (Figure 1b for isotherms, Supplementary Table 1 for textural parameters). The B-BNO sample displays a BET equivalent specific surface area of $18\text{ m}^2\text{ g}^{-1}$ and a total pore volume of $0.025\text{ cm}^3\text{ g}^{-1}$, which are considerably lower than those for porous BNO ($1585\text{ m}^2\text{ g}^{-1}$ and $1.10\text{ cm}^3\text{ g}^{-1}$). This is to be expected given the prolonged high temperature synthesis required to synthesize B-BNO and the lack of precursors in the synthesis that are capable of releasing gases to form pores. The type I/IV isotherm with a type H3/H4 hysteresis loop observed for porous BNO indicates the presence of slit-shaped micro- and mesopores.

We analyzed the chemical composition and bonding types of B-BNO using FT-IR and XPS (Figure 2 and Supplementary Figures 2 and 3) and compared them to those of porous BNO. Both samples exhibit the two characteristic IR bands of BN at $\sim 1380\text{ cm}^{-1}$ (in-plane B-N transverse stretching) and $\sim 800\text{ cm}^{-1}$ (out-of-plane B-N-B bending).⁵³ We also observed a weak B-O band at $\sim 1000\text{ cm}^{-1}$, which is not observed in B-BNO (Figure 2a).^{35, 43, 44} To gain further insight into the relative atomic surface composition and chemical states of the elements, we collected high resolution core level spectra through XPS. The fitted B 1s core level spectra for the starting amorphous boron precursor and the final B-BNO material are presented in Figure 2b. The complete fitted B 1s, N 1s and O 1s core level spectra for both B-BNO and porous BNO are presented in Supplementary Figures 2 and 3. The relative atomic compositions of both are presented in Supplementary Table 2. The key results from the XPS analysis are two-fold. Firstly, Figure 2c illustrates the complete nitrification of amorphous boron and incorporation of boron in the final B-BNO structure. Amorphous boron exhibits two peaks at binding energies of 187.6 eV, corresponding to B-B bonds in the icosahedral boron clusters, and 189.0 eV, corresponding to B-O bonds in oxides on the surface of the boron-rich clusters, where oxygen atoms are surrounded by several boron atoms ($\text{B}_x\text{-O}$).^{54, 55} Further, a small peak at 193.2 eV is observed in amorphous boron, corresponding to a surface layer of boron oxide (B_2O_3).⁵⁴ Amorphous boron has a near-zero nitrogen content, which is a valuable aid in quantifying the extent of nitrification and conversion to BN. Both the B-B peak at

187.6 eV and the B_x-O peak at 189.0 eV are not observed in the B 1s spectrum of the final B-BNO material. Instead, we observe a distinct peak at 191.0 eV, corresponding to the B-N bond,^{46,56,57} and a smaller peak at 192.3 eV that we attribute to the boron oxynitride (B-O_x-N_{3-x}) species, which stems from the in-plane substitution of oxygen atoms in the BN lattice, as we have described in a prior study.^{35,44} The B-N and B-O_x-N_{3-x} peaks at 191.0 eV and 192.3 eV (Figure 2a), respectively, as well as an increase of 42 at. % in the relative nitrogen content (Figure 2c) confirms the formation of a BN material. The absence of the B-B peak at 188.2 eV, as well as the increase in relative atomic composition of boron (Figure 2c), in the B-BNO material indicate that boron has been successfully doped into BNO and the nature of doping is random atomic substitution as opposed to island formation of boron clusters.

The formation of BN is also confirmed through the fitted core level spectra N 1s which show the presence of B-N bonds (398.5 eV for N 1s, Supplementary Figure 2).⁵⁷ We also observe shake-up satellite peaks in the B 1s and N 1s core level spectra for B-BNO (Supplementary Figure 2), which provides evidence for the formation of an sp²-hybridized hexagonal BN phase.^{58,59} We also note a small proportion of oxygen (3 at. %) in B-BNO with a peak at 192.3 eV and 533.1 eV for the B 1s and O 1s core level spectra, respectively, which we attribute to the aforementioned boron oxynitride (B-O_x-N_{3-x}) species. Whilst amorphous boron exhibited a relatively high carbon content (~ 13 at. %), the carbon content in the B-BNO sample was comparatively much lower (~1 at. %) and is linked to the presence of adventitious carbon impurities, *i.e.* not part of the material.

Next, we probed the optoelectronic properties of B-BNO through UV-vis diffuse reflectance spectroscopy. The absorption spectrum (Figure 2d) of the material clearly indicates a prominent red-shift when moving from porous BN to B-BNO, with an absorption edge shift from 320 nm to 730 nm. From the Tauc plot of the transformed Kubelka-Munk function against photon energy (Supplementary Figure 4), the B-BNO sample exhibits a deep visible band gap of 1.70 eV ± 0.05 eV, significantly lower than that of porous BNO (~3.55 eV ± 0.05 eV) (Supplementary Figure 4). We consider B-BNO and porous BNO as direct band-gap semiconductors based on literature.⁴⁷

In our previous study,³⁵ we were not able to infer whether the reduction in band gap from *h*-BN to porous BNO was related to the presence of functional groups, their specific location on the BN nanosheets or the introduction of porosity. However, the significant change in the semiconducting properties when transitioning from porous BNO to a non-porous B-BNO, suggests that this change can be attributed to the chemical modification, namely boron doping. We followed the same methodology as our previous study³⁵ to determine the band structure of B-BNO in comparison to porous BNO by measuring the valence band offset (ΔE_{VB}) and work function (Φ) through XPS measurements (Supplementary Figures 5 and 6). We note here that since the charge carriers are bound and trapped in a potential well, the energies relative to absolute vacuum are negative. Hence, the work function (Φ) and valence band offset (ΔE_{VB}) take negative values relative to absolute vacuum based on the notation outlined in our previous study.³⁵ B-BNO and porous BNO exhibited valence band offsets of -1.60 eV and -3.05 eV, respectively (Supplementary Figure 5). The work functions for B-BNO and porous BNO were determined to be -4.0 eV and -3.1 eV, respectively (Supplementary Figure 6).

By combining this data with the optical band gaps determined in Supplementary Figure 4, we determine the conduction and valence bands to be -3.90 eV and -5.60 eV for B-BNO and -2.60 eV and -6.15 eV for porous BNO. The complete band structures for B-BNO and porous BNO on the absolute energy scale vs. vacuum, with the redox potentials for H^+/H_2 , $TEOA^+/TEOA$, O_2/H_2O and CO_2/CO vs. SHE at pH = 7 are presented in Figure 2e. The conduction and valence bands for both B-BNO and porous BNO straddle the redox potentials for both the photoreforming of water and CO_2 photoreduction systems, which is imperative for the material to be able to thermodynamically facilitate the reaction. We observe that the separation between the Fermi level and conduction band in B-BNO is smaller as compared to porous BNO (Figure 2e). This suggests that B-BNO exhibits a stronger n-type character than porous BNO, which is desirable for both H_2 evolution and CO_2 photoreduction. The band positions of B-BNO and porous BNO in Figure 2e indicate that the formation of a composite BNO photocatalyst *via* a type I heterojunction might be possible to enhance charge separation.

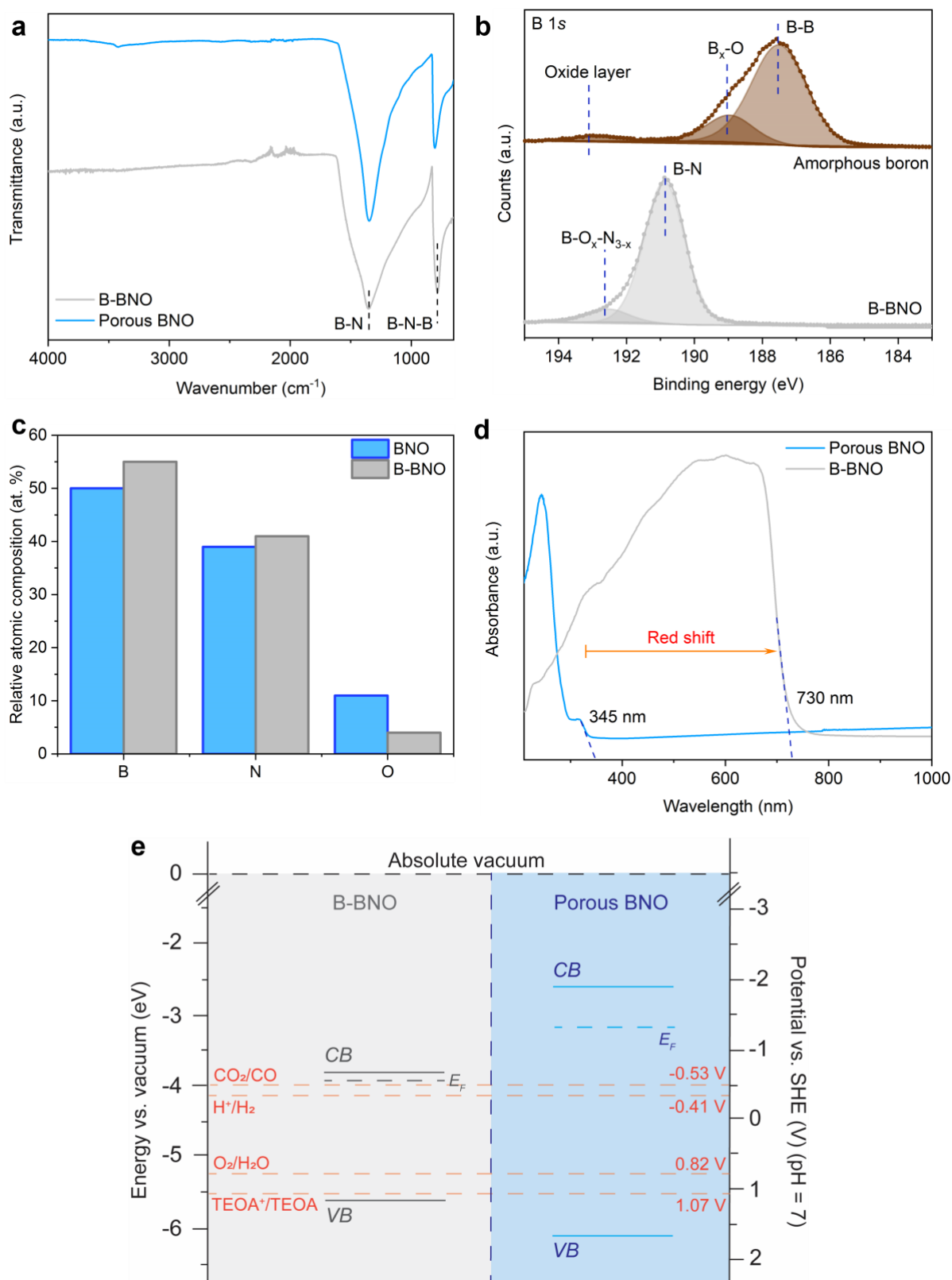


Figure 2 | Chemical, electronic and photophysical characterization of B-BNO and porous BNO. (a) FT-IR spectra of the as-synthesized B-BNO, with key characteristic bands highlighted, in comparison to porous BNO (b) Comparison of fitted B 1s core level spectra for

amorphous boron and B-BNO, (c) Relative atomic composition of B-BNO as obtained through XPS analysis, compared to porous BNO. (d) UV-Vis DRS absorption spectrum of the B-BNO sample compared to that of porous BNO, (e) Band structure for B-BNO and porous BNO on the absolute energy scale vs. vacuum with the conduction and valence bands, with the redox potentials for H^+/H_2 , O_2/H_2O , $TEOA^+/TEOA$ and CO_2/CO illustrated.

To investigate the paramagnetic species of the B-BNO compound, electron paramagnetic resonance (EPR) spectroscopy was used (Figure 3). The radical peak is attributed to the unpaired electron stemming from OB_3 sites, where an oxygen atom has substituted an interior nitrogen atom in the lattice and is surrounded by 3 neighbouring boron atoms.^{35, 43} The B-BNO radical peak is significantly enhanced in the EPR spectra compared to the porous BNO (Figure 3a). The g -values are also shifted between the two compounds, which is expected as g -values are highly sensitive to the chemical environment of radicals. Most importantly, fine structure features are apparent in the B-BNO spectrum, which can be attributed to hyperfine interactions. Hyperfine interactions refer to interactions between an unpaired electron and the nuclei of the surrounding neighbour atoms. Isotropic hyperfine interactions have previously been reported in BN based materials, where the unpaired electron stabilised in a nitrogen vacancy interacts with 3 boron nuclei.^{60, 61} The peak splitting observed in the B-BNO spectrum originates from 10 lines. Considering ^{11}B , the most abundant isotope of boron with $I = 3/2$, 3 boron nuclei must be interacting according to the $2NI + 1$ rule. A simulation with least square fitting was used to determine the hyperfine tensor (Figure 3b). The hyperfine tensor was found to have rhombic anisotropy, with an isotropic component $A_{iso} = 12$ MHz (0.43 mT) and an anisotropic dipolar component [10 -2 -8] MHz. Previous work has shown that BNO materials exhibit a planar system with the OB_3 radical in a $2p_z$ antibonding orbital.⁶² Our EPR results confirm that this is also what is observed here for B-BNO, as the hyperfine tensor is in line with what can be predicted for a H bound to a p-radical, such as CH_3 .⁶³ The unequivocal confirmation of isolated OB_3 sites as the radical species, which play an important role in extending the band gap to the deep visible range in BNO materials, verifies our previous hypothesis.³⁵

The presence of hyperfine interactions further provides direct insight into the chemical structure of the B-BNO material. A proposed structure for B-BNO is presented in Figure 3c. As the primary reactions are nitrification coupled with O/N substitution, it is likely that a nitrated surface layer of BNO is formed with the oxygen atoms substituting nitrogen atoms to form isolated OB_3 sites. We postulate that small clusters/chains of B-B bonds through B doping are formed in the bulk of the material and sporadically distributed. This, coupled with the low atomic content (~5 at. %, Figure 2c), could explain why B-B bonding is not detected for B-BNO *via* XPS, a surface sensitive technique. Alongside the isolated OB_3 sites, the small clusters of doped B-B bonds contribute to the lowering of the band gap in B-BNO to the deep visible range. Indeed, the presence of B-B chains can promote the formation of isolated OB_3 sites, as shown in Figure 3c. With the aforementioned reactions, the nitrogen and oxygen atoms are competing for bonding sites to the boron atoms. An oxygen atom being embedded within the B-B chains leads to the formation of isolated OB_3 sites and would result in the hyperfine interactions observed in Figures 3a and 3b. The lower oxygen content in B-BNO compared to porous BNO (see Figure 2c), coupled with the increased boron content through B-B chains, in B-BNO promotes the formation of isolated OB_3 states. Higher oxygen contents, as in porous BNO, can increase the likelihood of forming conjugated O-B-O chains *via* adjacent OB_3 states, which is a diamagnetic state that does not contribute to the EPR signal.^{35, 43} Hence, boron doping has a dual effect on the photochemistry of B-BNO, which extends light harvesting to the deep visible range.

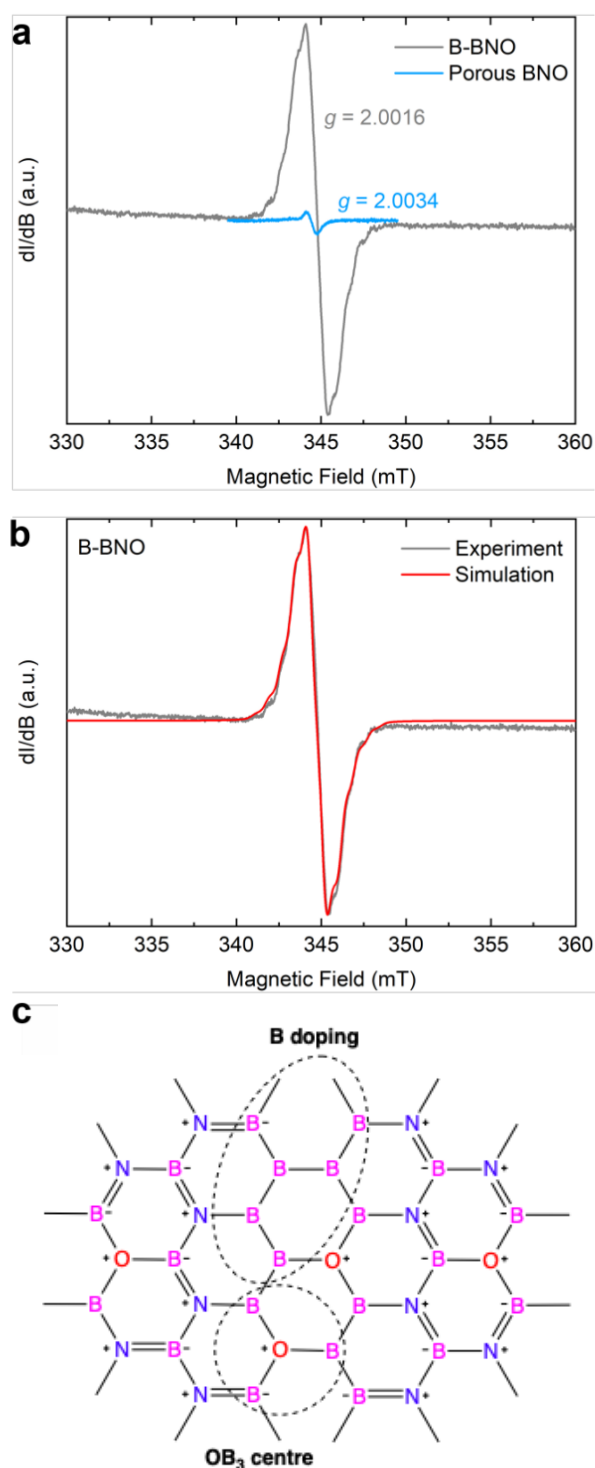


Figure 3 | Paramagnetic characterisation of B-BNO compared to porous BNO. (a) Room temperature EPR spectra for B-BNO compared to the porous BNO used as reference with the g -values indicated, (b) Simulation of the EPR spectra for B-BNO showing hyperfine interactions, (c) Schematic for the proposed B-BNO structure highlighting the B-B chains and the isolated OB_3 sites yielding hyperfine interactions shown.

Next, we tested B-BNO as a photocatalyst to facilitate hydrogen evolution *via* the photoreforming of water under UV-Vis and pure deep visible ($\lambda > 550$ nm) irradiation, in a 0.1 M TEOA (aq) solution, without the presence of a co-catalyst (Figure 4). The performance was compared to 'reference' materials, *i.e.* P25 TiO₂ and bulk graphitic carbon nitride (g-C₃N₄). P25 TiO₂ is a benchmark commercial material in the field, which enables comparison with other groups' work, despite differences in experimental set-ups. Being a commercial material, P25 acts as an internal reference and its use for comparison is in part of the guidance in the field.⁶⁴ Graphitic carbon nitride is the closest material in terms of chemistry and structure to boron nitride and a well-known visible light photocatalyst for H₂ evolution and CO₂ photoreduction.⁶⁵ Under the conditions, B-BNO drove the photoreforming of water with an average specific H₂ production rate of 241.45 $\mu\text{mol g}^{-1} \text{h}^{-1}$ under UV-Vis irradiation and 12.35 $\mu\text{mol g}^{-1} \text{h}^{-1}$ under pure deep visible irradiation ($\lambda > 550$ nm). P25 TiO₂ and bulk g-C₃N₄ yielded an average specific H₂ production rate of 74.75 $\mu\text{mol g}^{-1} \text{h}^{-1}$ and 6.25 $\mu\text{mol g}^{-1} \text{h}^{-1}$ under UV-Vis irradiation, which shows that B-BNO has a substantially higher photocatalytic output over the full UV-Vis spectrum than the reference materials. The quantum efficiency (QE) (*i.e.* over the entire irradiation spectrum) for B-BNO was determined to be 0.01% across the full UV-Vis spectrum of the Xe arc lamp source (270 – 900 nm) and $1.5 \times 10^{-3}\%$ in the deep visible region of the spectrum (550 – 900 nm) (see Supplementary Information for calculation procedure and error analysis). The QE of B-BNO for H₂ evolution was more than double that of P25 TiO₂ ($4.4 \times 10^{-3}\%$) and an order of magnitude higher than bulk g-C₃N₄ ($9.2 \times 10^{-4}\%$). The specific H₂ evolution rates and quantum efficiencies of all the materials investigated in this study are tabulated in Supplementary Table 3. None of the reference materials exhibited any photoactivity under deep visible irradiation ($\lambda > 550$ nm), which is to be expected given their higher band gaps (3.55 eV, 3.20 eV and 2.72 eV for porous BNO, P25 TiO₂, and bulk g-C₃N₄ respectively). Hence, B-BNO offers both a wider and greater light harvesting efficiency than porous BNO and reference materials for H₂ evolution *via* photoreforming of water. To assess the source of protons, we used D₂O as the solvent, whilst maintaining the same catalyst preparation method and reaction conditions from the original system. When D₂O was used instead of H₂O, only D₂

was detected under mass spectrometry (Supplementary Figure 7). The results indicate that water serves as the proton source and TEOA acts as the electron donor. B-BNO maintained its photoactivity over a 10-hour testing period (see kinetic study, Figure 4b).

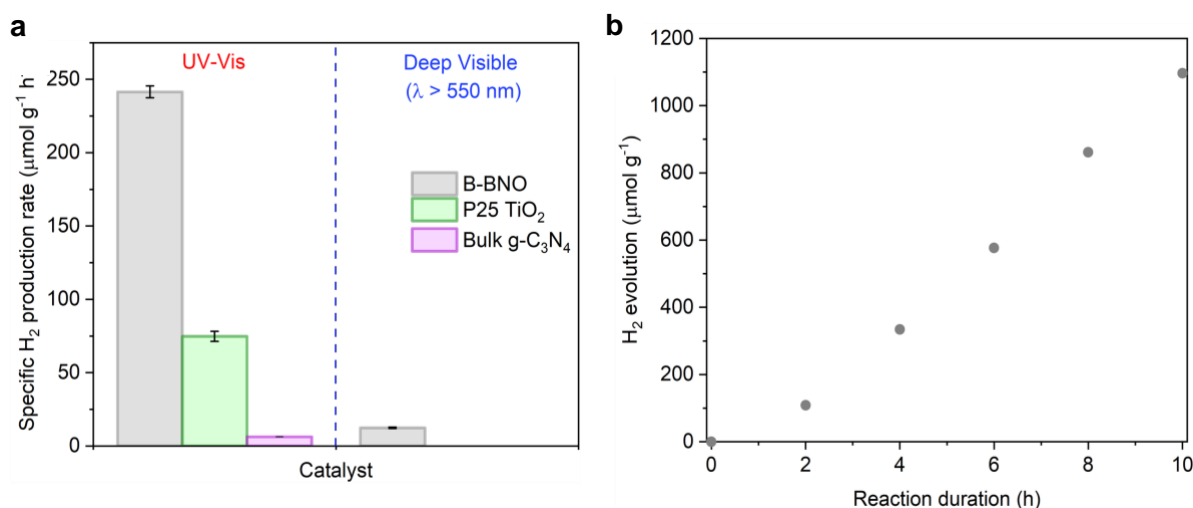


Figure 4 | Photocatalytic testing of B-BNO for H₂ evolution through photoreforming of water. (a) Specific production rate of H₂ for B-BNO compared to P25 TiO₂, and bulk carbon nitride (g-C₃N₄) as reference materials, under UV-Vis and pure deep visible light irradiation (λ > 550 nm) and 0.1 M TEOA (aq) sacrificial donor solution (300 W Xe arc lamp, 12.5 cm distance from catalyst to lamp source, 3 hours, 25 °C). Average intensity at the catalyst surface was 1730 ± 26 W m⁻² without the UV-filter and 1530 ± 12 W m⁻² with the deep visible filter (λ > 550 nm), (b) Kinetic study illustrating photocatalytic H₂ evolution from B-BNO as a function of time under UV-Vis irradiation (same lamp, intensity and reactor settings as before).

We subsequently investigated whether B-BNO could function as a multifunctional photocatalyst and facilitate combined CO₂ capture and photoreduction in the gas phase. The results from our previous study³⁵ would lead us to believe that a high surface area and porosity, as observed in porous BNO, would be required to facilitate this process. However, although B-BNO lacks surface area and porosity compared to its porous counterpart, testing the material for combined CO₂ capture and photoreduction in the gas phase can provide some insight into the role of porosity in BN photocatalysts and indicate whether the enhanced light harvesting capability can compensate

for a potential loss in CO₂ adsorption. Moreover, several photocatalysts being tested in the literature for CO₂ photoreduction are non-porous yet show photocatalytic output. Prior to photocatalytic testing, we measured the CO₂ adsorption capacity of the material at the reaction conditions (25 °C, 0-1 bara) and compared to porous BNO and the 'reference' materials, *i.e.* P25 TiO₂ and carbon nitride. Unsurprisingly, porous BNO adsorbs significantly more CO₂ than B-BNO and the reference materials (Figure 5a, Supplementary Table 4), due to its higher porosity (Supplementary Table 1). Next, we tested B-BNO, porous BNO and the reference materials for the gas phase photoreduction of CO₂ under UV-vis and pure deep visible irradiation ($\lambda > 550$ nm), without doping or the presence of a co-catalyst. H₂ was used for the oxidation half-reaction. For all materials, after an irradiation time of 3 hours, CO was observed as the major product, with comparatively smaller quantities of CH₄ detected. Under these conditions, B-BNO drove the photoreduction of CO₂ with an average specific CO production rate of 6.53 $\mu\text{mol g}^{-1} \text{h}^{-1}$ and a QE of $1.3 \times 10^{-3}\%$ across the UV-Vis spectrum (270 – 900 nm), which was almost order of magnitude higher than that of porous BNO (CO production rate of 0.61 $\mu\text{mol g}^{-1} \text{h}^{-1}$ and QE of $7.6 \times 10^{-5}\%$). B-BNO also exhibited a higher specific CO production rate and QE than those for the reference materials (1.01 $\mu\text{mol g}^{-1} \text{h}^{-1}$ for P25 TiO₂ and 0.30 $\mu\text{mol g}^{-1} \text{h}^{-1}$ for bulk g-C₃N₄). The same trend amongst the materials is also observed with regard to the minor product, CH₄ (Figure 5b and Supplementary Table 4). Further, B-BNO also exhibited the highest selectivity towards CO production (94.2 %) amongst the materials tested in this study (Supplementary Table 5). The specific CO and CH₄ evolution rates, QEs and selectivities of all the materials investigated in this study are tabulated in Supplementary Tables 4 and 5, respectively. We note that porous BNO indeed displayed a higher specific CO production rate compared to P25 TiO₂ in our previous study.³⁵ A possible cause for this variation in trend could be the change in intensity and spread of the incident light irradiation on the material between the two studies. Overall, the results suggest that the extended light absorption to the deep visible range in B-BNO compensates the lower porosity and surface area. The difference in photophysics observed in Figure 3 between B-BNO and porous BNO may have influence as well.

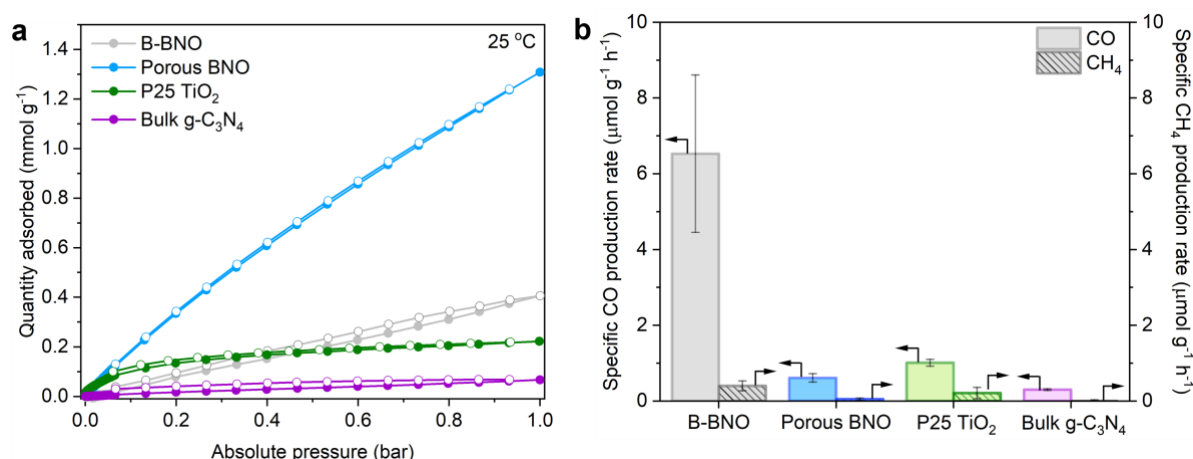


Figure 5 | Photocatalytic testing of B-BNO for gas phase CO₂ photoreduction. (a) CO₂ adsorption isotherms collected at 25 °C for the materials investigated in this study, (b) Specific production rates of CO and CH₄ for B-BNO, compared to porous BNO, P25 TiO₂, bulk carbon nitride (g-C₃N₄), as reference materials, under UV-vis irradiation and H₂ as a sacrificial agent (300 W Xe arc lamp, 9.5 cm distance from catalyst to lamp source, 3 hours, 25 °C). Intensity at the catalyst surface was $1850 \pm 17 \text{ W m}^{-2}$.

To confirm the origin of CO, we carried out isotopic experiments using ¹³CO₂. Aside from ¹³CO₂ being used as the feed gas in tandem with H₂ as the sacrificial agent, we maintained the same catalyst preparation method and reaction conditions from the original system. The gas chromatograms corresponding to the ¹³CO peak (*m/z* = 29) and ¹²CO (*m/z* = 28) under both dark and light conditions, as well as the mass spectra for the photocatalytic ¹³CO₂ reduction system are presented in Supplementary Figure 8. Here, ‘dark’ and ‘light’ refer to the pre- and post-reaction conditions. Under dark conditions, no ¹²CO nor ¹³CO is observed in the system. Under light conditions after the completion of the reaction, only ¹³CO (*m/z* = 29) is observed in the gas chromatogram, with no peak for ¹²CO (*m/z* = 28) observed. In accordance with this is the corresponding mass spectra that shows *m/z* = 45 (¹³CO₂) and *m/z* = 29 (¹³CO) are the dominant peaks. The results point to the formation of ¹³CO and provides direct evidence that the origin of the evolved CO is indeed from the reduction of CO₂ itself.

Conclusions

In summary, we present a step-change in the family of boron oxynitride materials by introducing the first example of a B-doped boron oxynitride (B-BNO). This material exhibits unique semiconducting properties and photophysics, with hyperfine interactions between the unpaired electron from oxygen atoms and the nuclear spin of neighbouring boron atoms observed through room temperature EPR spectra. The results confirm that the paramagnetic signature originates from isolated OB_3 sites, which play an important role in extending the band gap to the deep visible range in BNO materials. The presence of hyperfine interactions further provides direct insight into the structure and chemistry of B-BNO material, as well as the symmetry of the radical. We show that B-BNO can address a bottleneck associated to the benchmark BN photocatalyst, porous BNO, namely the lack of light harvesting in the visible region. In doing so, B-BNO can facilitate H_2 evolution *via* the photoreforming of water under a simple solid/liquid phase set-up under ambient conditions with a QE of 0.01%, and without the use of co-catalysts. This photocatalytic output and quantum efficiency are at least two orders of magnitude higher than porous BNO and bulk $g-C_3N_4$, and three times higher than benchmark in the field, *i.e.* P25 TiO_2 . B-BNO exhibits a steady H_2 evolution rate over a single cycle. In addition, B-BNO can serve as a multifunctional photocatalyst and photoreduce CO_2 to CO and CH_4 , with a 92.4% CO selectivity and QE of $1.3 \times 10^{-3}\%$, in the gas phase. Again the evolution rates, CO selectivities and quantum efficiencies significantly exceed those of porous BNO, P25 TiO_2 and bulk $g-C_3N_4$.

Acknowledgements

The authors would like to acknowledge the funding from EPSRC through the Doctoral Partnership fund (1855454), which made this research possible, and through the EPSRC equipment funding for SPIN-Lab (EP/P030548/1), as well as ERC Starting Grant THEIA (Project Number: 850624).

Declaration

The authors declare that there are no competing financial interests.

References

1. IEA, *World Energy Outlook*, 2019.
2. J. A. Herron, J. Kim, A. A. Upadhye, G. W. Huber and C. T. Maravelias, *Energy Environ. Sci.*, 2015, **8**, 126-157.
3. S. Zhang, Y. Zhao, R. Shi, C. Zhou, G. I. Waterhouse, L. Z. Wu, C. H. Tung and T. Zhang, *Adv. Energy Mater.*, 2020, **10**, 1901973.
4. Z.-K. Shen, Y. Yuan, P. Wang, W. Bai, L. Pei, S. Wu, Z. Yu and Z. Zou, *ACS Appl. Mater. Interfaces*, 2020, **12**, 17343-17352.
5. H.-i. Kim, Y. Choi, S. Hu, W. Choi and J.-H. Kim, *Appl. Catal. B*, 2018, **229**, 121-129.
6. A. Fujishima and K. Honda, *Nature*, 1972, **238**, 37-38.
7. T. Inoue, A. Fujishima, S. Konishi and K. Honda, *Nature*, 1979, **277**, 637-638.
8. A. Crake, K. C. Christoforidis, A. Kafizas, S. Zafeiratos and C. Petit, *Appl. Catal. B*, 2017, **210**, 131-140.
9. A. Crake, K. C. Christoforidis, R. Godin, B. Moss, A. Kafizas, S. Zafeiratos, J. R. Durrant and C. Petit, *Appl. Catal. B*, 2019, **242**, 369-378.
10. A. Crake, K. C. Christoforidis, A. Gregg, B. Moss, A. Kafizas and C. Petit, *Small*, 2019, **15**, 1805473.
11. T. W. Woolerton, S. Sheard, E. Pierce, S. W. Ragsdale and F. A. Armstrong, *Energy Environ. Sci.*, 2011, **4**, 2393-2399.
12. T. W. Woolerton, S. Sheard, E. Reiser, E. Pierce, S. W. Ragsdale and F. A. Armstrong, *J. Am. Chem. Soc.*, 2010, **132**, 2132-2133.
13. F. Liao, Z. Zeng, C. Eley, Q. Lu, X. Hong and S. C. E. Tsang, *Angew. Chem. Int. Ed.*, 2012, **51**, 5832-5836.
14. H. Lin, Y. Liu, J. Deng, S. Xie, X. Zhao, J. Yang, K. Zhang, Z. Han and H. Dai, *J. Photochem. Photobiol*, 2017, **336**, 105-114.
15. J. Nunez, A. Víctor, P. Jana, J. M. Coronado and D. P. Serrano, *Catal. Today*, 2013, **209**, 21-27.
16. F. Yoshitomi, K. Sekizawa, K. Maeda and O. Ishitani, *ACS Appl. Mater. Interfaces*, 2015, **7**, 13092-13097.
17. N. Zhang, S. Ouyang, T. Kako and J. Ye, *ChemComm*, 2012, **48**, 1269-1271.
18. Y. P. Xie, G. Liu, G. Q. M. Lu and H.-M. Cheng, *Nanoscale*, 2012, **4**, 1267-1270.
19. Y. Cao, R. Zhang, T. Zhou, S. Jin, J. Huang, L. Ye, Z. Huang, F. Wang and Y. Zhou, *ACS Appl. Mater. Interfaces*, 2020, **12**, 9935-9943.
20. S. Zhou, Y. Liu, J. Li, Y. Wang, G. Jiang, Z. Zhao, D. Wang, A. Duan, J. Liu and Y. Wei, *Appl. Catal. B*, 2014, **158**, 20-29.
21. M. Zhou, S. Wang, P. Yang, C. Huang and X. Wang, *ACS Catal.*, 2018, **8**, 4928-4936.
22. Z. Sun, J. M. T. A. Fischer, Q. Li, J. Hu, Q. Tang, H. Wang, Z. Wu, M. Hankel, D. J. Searles and L. Wang, *Appl. Catal. B*, 2017, **216**, 146-155.
23. J. Lin, Z. Pan and X. Wang, *ACS Sustain. Chem. Eng.*, 2013, **2**, 353-358.
24. Y. Zhang and M. Antonietti, *Chem. Asian J.*, 2010, **5**, 1307-1311.
25. L. Acharya, S. Nayak, S. P. Pattnaik, R. Acharya and K. Parida, *J. Colloid Sci.*, 2020, **566**, 211-223.
26. M. Campanelli, T. Del Giacco, F. De Angelis, E. Mosconi, M. Taddei, F. Marmottini, R. D'Amato and F. Costantino, *ACS Appl. Mater. Interfaces*, 2019.
27. S. Yang, W. Hu, X. Zhang, P. He, B. Pattengale, C. Liu, M. Cendejas, I. Hermans, X. Zhang and J. Zhang, *J. Am. Chem. Soc.*, 2018, **140**, 14614-14618.

28. M. Lu, J. Liu, Q. Li, M. Zhang, M. Liu, J. L. Wang, D. Q. Yuan and Y. Q. Lan, *Angew. Chem.*, 2019, **131**, 12522-12527.
29. W. Zhong, R. Sa, L. Li, Y. He, L. Li, J. Bi, Z. Zhuang, Y. Yu and Z. Zou, *J. Am. Chem. Soc.*, 2019, **141**, 7615-7621.
30. R. S. Sprick, B. Bonillo, R. Clowes, P. Guiglion, N. J. Brownbill, B. J. Slater, F. Blanc, M. A. Zwijnenburg, D. J. Adams and A. I. Cooper, *Angew. Chem. Int. Ed.*, 2016, **55**, 1792-1796.
31. M. Sachs, R. S. Sprick, D. Pearce, S. A. Hillman, A. Monti, A. A. Guilbert, N. J. Brownbill, S. Dimitrov, X. Shi and F. Blanc, *Nat. Commun.*, 2018, **9**, 1-11.
32. R. S. Sprick, B. Bonillo, M. Sachs, R. Clowes, J. R. Durrant, D. J. Adams and A. I. Cooper, *ChemComm*, 2016, **52**, 10008-10011.
33. L. Wang, R. Fernández-Terán, L. Zhang, D. L. Fernandes, L. Tian, H. Chen and H. Tian, *Angew. Chem. Int. Ed.*, 2016, **55**, 12306-12310.
34. X. Jin, Q. Guan, T. Tian, H. Li, Y. Han, F. Hao, Y. Cui, W. Li, Y. Zhu and Y. Zhang, *Appl. Surf. Sci.*, 2020, **504**, 144241.
35. R. Shankar, M. Sachs, L. Francàs, D. Lubert-Perquel, G. Kerherve, A. Regoutz and C. Petit, *J. Mater. Chem. A*, 2019, **7**, 23931-23940.
36. M. Wang, M. Li, L. Xu, L. Wang, Z. Ju, G. Li and Y. Qian, *Catal. Sci. Technol.*, 2011, **1**, 1159-1165.
37. X. Li, J. Zhao and J. Yang, *Sci. Rep.*, 2013, **3**, 1858.
38. J. Pang, Y. Chao, H. Chang, H. Li, J. Xiong, M. He, Q. Zhang, H. Li and W. Zhu, *J. Colloid Sci.*, 2017, **508**, 121-128.
39. X. Wang, K. Maeda, A. Thomas, K. Takanebe, G. Xin, J. M. Carlsson, K. Domen and M. Antonietti, *Nat. Mater.*, 2009, **8**, 76.
40. C. Huang, C. Chen, M. Zhang, L. Lin, X. Ye, S. Lin, M. Antonietti and X. Wang, *Nat. Commun.*, 2015, **6**, 7698.
41. Q. Weng, Y. Ide, X. Wang, X. Wang, C. Zhang, X. Jiang, Y. Xue, P. Dai, K. Komaguchi and Y. Bando, *Nano Energy*, 2015, **16**, 19-27.
42. Z. He, C. Kim, L. Lin, T. H. Jeon, S. Lin, X. Wang and W. Choi, *Nano Energy*, 2017, **42**, 58-68.
43. Q. Weng, D. G. Kvashnin, X. Wang, O. Cretu, Y. Yang, M. Zhou, C. Zhang, D. M. Tang, P. B. Sorokin and Y. Bando, *Adv. Mater.*, 2017, **29**, 1700695.
44. R. Shankar, S. Marchesini and C. Petit, *J. Phys. Chem. C*, 2019, **123**, 4282-4290.
45. L. Rusanova and L. Gorchakova, *J. Sov. Powder Metall. Met. Ceram.*, 1980, **19**, 189-191.
46. S. Marchesini, A. Regoutz, D. Payne and C. Petit, *Microporous Mesoporous Mater.*, 2017, **243**, 154-163.
47. K. Watanabe, T. Taniguchi and H. Kanda, *Nat. Mater.*, 2004, **3**, 404-409.
48. S. Brunauer, P. H. Emmett and E. Teller, *J. Am. Chem. Soc.*, 1938, **60**, 309-319.
49. S. Chen and R. Yang, *Langmuir*, 1994, **10**, 4244-4249.
50. S. Stoll and A. Schweiger, *J. Magn. Reson.*, 2006, **178**, 42-55.
51. O. O. Kurakevych and V. L. Solozhenko, *Acta Crystallogr. C*, 2007, **63**, i80-i82.
52. S. Marchesini, C. M. McGilvery, J. Bailey and C. Petit, *ACS Nano*, 2017, **11**, 10003-10011.
53. R. Geick, C. Perry and G. Rupprecht, *Phys. Rev.*, 1966, **146**, 543.
54. G. Liu, L. C. Yin, P. Niu, W. Jiao and H. M. Cheng, *Angew. Chem. Int. Ed.*, 2013, **52**, 6242-6245.
55. Q. Fan, C. Choi, C. Yan, Y. Liu, J. Qiu, S. Hong, Y. Jung and Z. Sun, *ChemComm*, 2019, **55**, 4246-4249.
56. G. Ciofani, G. G. Genchi, I. Liakos, A. Athanassiou, D. Dinucci, F. Chiellini and V. Mattoli, *J. Colloid Sci.*, 2012, **374**, 308-314.
57. V. Cholet, L. Vandenbulcke, J. Rouan, P. Baillif and R. Erre, *J. Mater. Sci.*, 1994, **29**, 1417-1435.
58. K. Park, D. Lee, K. Kim and D. Moon, *Appl. Phys. Lett.*, 1997, **70**, 315-317.
59. A. S. Nazarov, V. N. Demin, E. D. Grayfer, A. I. Bulavchenko, A. T. Arymbaeva, H. J. Shin, J. Y. Choi and V. E. Fedorov, *Chem. Asian J.*, 2012, **7**, 554-560.
60. V. I. Matkovich, G.-. Samsonov and P. Hagemuller, *Boron and refractory borides*, Springer, 1977.

61. A. Panich, A. Shames, N. Froumin, C. Tang and Y. Bando, *Phys. Rev. B*, 2005, **72**, 085307.
62. K. Simonov, N. A. Vinogradov, M. L. Ng, A. Vinogradov, N. Mårtensson and A. Preobrajenski, *Surf. Sci.*, 2012, **606**, 564-570.
63. F. Gerson and W. Huber, *Electron spin resonance spectroscopy of organic radicals*, John Wiley & Sons, 2003.
64. M. Marszewski, S. Cao, J. Yu and M. Jaroniec, *Mater. Horiz*, 2015, **2**, 261-278.
65. G. Liao, Y. Gong, L. Zhang, H. Gao, G.-J. Yang and B. Fang, *Energy Environ. Sci.*, 2019, **12**, 2080-2147.